Published by IOP Publishing for Sissa Medialab

Received: *December 13, 2019*
Revised: *January 31, 2020*
Accepted: *February 22, 2020*
Published: *April 2, 2020*

A mini-imaging air Cherenkov Telescope

S.N. Ekoume,[a] C. Alispach,[a] F. Cadoux,[a] V. Coco,[a] D. della Volpe,[a] Y. Favre,[a] M. Heller,[a,1] T. Montaruli,[a] A. Nagai,[a] A. Neronov,[b] Y. Renier[a] and I. Troyano,[a]

[a] *Département de physique nucléaire et corpusculaire, Faculté de Sciences, Université de Genève, 24 Quai E. Ansermet, Genève CH-1211 Switzerland*
[b] *Astronomy Department, University of Geneva, Ch. d'Ecogia 16, Versoix 1290, Switzerland*

E-mail: matthieu.heller@unige.ch

Abstract: In this paper we describe the different software and hardware elements of a mini-telescope for the detection of cosmic rays and gamma-rays using the Cherenkov light emitted by their induced particle showers in the atmosphere. We estimate the physics reach of the standalone mini-telescope and present some results of the measurements done at the Sauverny Observatory of the University of Geneva and at the Saint-Luc Observatory. These measurements demonstrate the ability of the telescope to observe cosmic rays with energy above about 100 TeV. Such a mini-telescope can constitute a cost-effective out-trigger array that can surround other gamma-ray telescopes or extended air showers detector arrays. Its development was born out of the desire to illustrate to students and amateurs the cosmic ray and gamma-ray detection from ground, as an example of what is done in experiments using larger telescopes. As a matter of fact, a mini-telescope can be used in outreach night events. While outreach is becoming more and more important in the scientific community to raise interest in the general public, the realisation of the mini-telescope is also a powerful way to train students on instrumentation such as photosensors, their associated electronics, acquisition software and data taking. In particular, this mini-telescope uses silicon photomultipliers (SiPM) and the dedicated ASIC, CITIROC.

Keywords: Cherenkov detectors; Detector design and construction technologies and materials; Gamma telescopes; Data acquisition circuits

ArXiv ePrint: 1912.05894

[1] Corresponding author.

https://doi.org/10.1088/1748-0221/15/04/P04004

2020 JINST 15 P04004

Contents

2020 JINST 15 P04004

1 Introduction

High-energy cosmic particles, called “primary” cosmic rays, interacting with atmospheric nuclei, produce showers of “secondary” particles of lower energies [1]. This multiplicative phenomenon occurs until the interacting particles reach a “critical energy” (of about 80 MeV for electrons in the atmosphere), when ionization losses take over energy losses through particle production. When a charged particle passes through the atmosphere with a velocity greater than the speed of light in air

($v > c/n_{\mathrm{air}}(h)$ or $\beta > 1/n_{\mathrm{air}}(h)$, where h is the altitude from the earth surface and n the refractive index of the atmosphere), Cherenkov radiation is emitted. This is due to the asymmetric polarization of the medium in the front and in the rear of the particle giving rise to a varying electric dipole momentum. This fast variation of the electromagnetic field generates real photons. The emitted Cherenkov radiation forms a light cone around the particle direction, whose aperture is about 1° in the atmosphere, increasing to about 1.3° close to the earth surface due the variation of $n_{\mathrm{air}}(h)$. The light pool exact size and intensity profile depend on the primary particle type, the height of production of the shower, the direction of the primary and the height of the detector location [2]. The Cherenkov light, emitted in flashes of a few nanoseconds, can be focused by means of mirrors or lenses on the detector plane of an Imaging Atmospheric Cherenkov Telescopes (IACTs). A camera on this plane, composed by many pixels with (sub-)nanosecond timing capabilities, can produce a snapshot of this fast flash of mainly blue and near-UV light. Since electromagnetic and hadronic showers have different structures and develop differently, cosmic rays can be discriminated from gamma-rays by means of their induced shower image on the camera. When an IACT points towards a gamma-ray source, electromagnetic showers appear as an elongated ellipsoid with its major axis pointing to the centre of the camera. This axis also defines their arrival direction. On the other hand, hadronic showers will produce blurred images, sometimes displaying rings due to muons. The energy of the primary particle is inferred by the charge collected in each pixel. To make a calorimetric measurement possible, the shower must reach its maximum development before reaching the telescope on ground, so that the Cherenkov emission reflects the number of charged particles in the shower, which is proportional to the primary energy. The determination of the shower parameters can be improved with a network of telescopes, when they are synchronized at ns-precision level and detect the same shower.

Following the first detection of the Crab Nebula in 1989 by Whipple [3], the second generation of IACTs, like H.E.S.S. [4], MAGIC [5], and VERITAS [6], have shown remarkable results and discoveries of several sources, such as the recent discovery of gamma-ray bursts [7–9] and the sources in the TeVCat catalog [10, 11]. Nonetheless, the IACT technique has some limitations, namely concerning the field of view limited to $\lesssim 10°$ and the observation time limited to $\sim 10\%$ of clear moonless nights (duty cycle). In the next future, the Cherenkov Telescope Array Observatory will be the largest ground-based observatory composed of two arrays of IACTs at the ESO site of Paranal and at La Palma, Canary Islands. The Cherenkov Telescope Array Observatory will serve as an open-access observatory to a wide astrophysics community and will provide deep insights into the non-thermal high-energy universe [12, 13]. One of the telescopes that was proposed for the implementation of the small size telescopes at the Southern array, is the single mirror small size telescope (SST-1M) [14, 15]. It adopts a Davies-Cotton optics with a single mirror with focal length of 5.6 m. The SST-1M has a field of view of 9° provided by a SiPM-based camera with 1296 pixels. These are composed by a custom-designed large hexagonal SiPM coupled with a hexagonal light funnel [16]. More details on the SST-1M photo-detection plane can be found in [15].

In this paper, we propose a mini-telescope with a simple and inexpensive design, that would complement IACT arrays of Cherenkov extensive air showers (e.g. HAWC [17] or LHAASO [18]), constituting an out-trigger array for improving particle identification and reconstruction capabilities. The mini-telescope design is described in section 2 while the calibration of the prototype is covered in section 3. Finally, the observations campaigns and the results are described in section 4.

2020 JINST 15 P04004

Complementary calculations to evaluate the physics reach of such a telescope are presented in appendix A and B.

2 The mini-telescope

The peculiarity of the mini-telescope described in this paper lies in utilising a lense combined with a SiPM-based camera, that makes it a very easy-to-build and inexpensive solution for a small IACT. A previous concept using a lens exists [19], but using photo-multipliers. Many of the constituents used for the assembly of the mini-telescope, except for the structure, had already been developed for other experiments: the Fresnel lens by the JEM-EUSO experiment [20], the optical modules by the single mirror small-sized telescope [21] for the Cherenkov Telescope Array [12] and the readout for the BabyMind experiment [22]. The full mini-telescope would take only a few months of work to be reproduced. Having reused most of the components, the design of the mini-telescope was constrained by these available components. Main characteristics are shown in table 1 and compared to the characteristics of the SST-1M telescope.

Table 1. Main characteristics of the mini-telescope compared to the SST-1M telescope. The angular pixel size (in radians) is the ratio between the linear pixel size and the focal length. The SST-1M and the mini-telescope use the same pixels but the difference in focal length between the two telescopes leads to a different angular pixel size. The field of view is the square root of the number of pixels multiply by the angular pixel size in degree.

	mini-telescope	SST-1M
Optics	Fresnel lens	Davies-Cotton
Collection area [m^2]	0.8	6.5
Focal length [m]	2.4	5.6
Field of View [°]	6.6	8.6
Linear pixel size [m]	0.234	0.234
Angular pixel size [°]	0.55	0.24
Number of pixels	144	1296
Electronics coupling	AC	DC
Readout	Peak sensing	Full waveform

Figure 1 presents a simplified functional diagram of the mini-telescope. The Cherenkov photons enter the telescope by the Fresnel lens and go through 2.4 m of air inside the telescope before reaching the protection window of the camera. The photons are guided to the SiPMs using hollow light-guides. The light-guides have been developed to increase the detection area of SiPMs and to limit the light angular acceptance to 24° [16]. The sensors, has been developed by the University of Geneva group in collaboration with Hamamatsu [23] and commercialized as the S12516-050 Multi Pixel Photon Counter. The SiPMs are coupled to a preamplifier board and a slow control board as in the SST-1M camera [15, 24]. If photons are detected, a current is generated by the SiPM and amplified in the SST-1M preamplifier board, providing a DC coupled differential output. The acquisition system consists of two Front-End Boards (FEB) each hosting three CITIROC ASICs [25]. The FEB is designed for the data readout system of the BabyMind

2020 JINST 15 P04004

Project [22, 26, 27], which is the muon spectrometer of the WAGASCI experiment at J-PARC [28]. Because the differential output is not compatible with the input stage of the BabyMind front-end board, an adaptation board was produced that matches the impedance of the preamplifier output and the FEB input. The board has three outputs per pixel: the time at which the event was triggered and the high and low gain detected signal. These information are transferred via USB3 to the data acquisition server where it is saved on disk.

We describe all components in detail below.

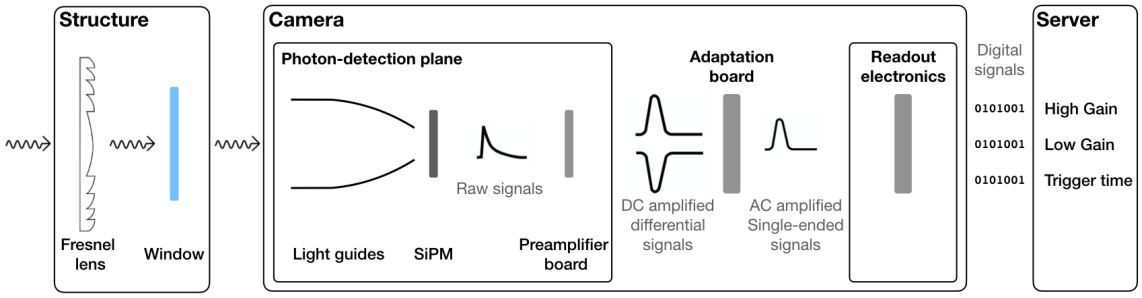

Figure 1. Simplified functional diagram of the mini-telescope for a single camera channel. The main components of its design are the structure which hold the Fresnel lens, the camera which transforms a photon flux into a digital information flow and finally the data acquisition server.

2.1 The support structure

The telescope structure is a 2.4 m long parallelepiped with a base of 1 m × 1 m to match the dimensions of the Fresnel lens. The structure is made out of 2 cm × 2 cm soldered aluminum beams. The side panels, also made out of aluminum, are riveted to the structure and covered with a matt black paint to avoid light reflection. A silicon joint is added between the side panels and the structure for the light tightness. One of the side panel can be removed in order to access the camera from the front-side for inspecting and mounting. The Fresnel lens is mounted on a frame which is attached to the structure using four bolts. In order to adjust the focal point, the bolts are coupled to nuts which allow a coarse positioning. The weight of the structure together with the Fresnel lens is about 50 kg.

The mini-camera, which has an hexagonal shape of 30 cm flat-to-flat, is installed at the bottom of the structure together with the readout electronics (in the back of the box in the CAD picture in figure 2-left).

The structure of the mini-telescope is mounted on a mobile base through a pivot allowing to rotate it from the horizon to the zenith (see figure 2-right) in order to observe at different elevation angles and be able to point at sources. An upgrade of the rotation system is possible to use a linear actuator that can be remotely controlled. The structure was designed and produced by the Sauverny Observatory of the Department of Astronomy of the University of Geneva.

2.2 The Fresnel lens

The UV-sensitive Fresnel lens is made of a 2 mm thick polymethyl-methacrylate sheet. It has a focal length of 2.4 m and an area of about 1 m^2. It is a prototype built for the Jem-EUSO collaboration, a

2020 JINST 15 P04004

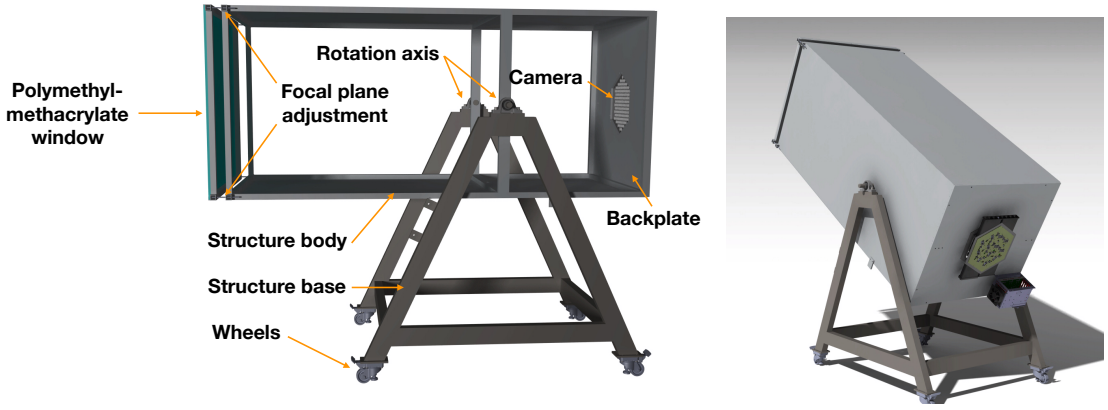

Figure 2. CAD drawings of the structure of the mini-telescope. Left: view of the mini-telescope structure from the side and without the side panels. The main components and dimension are indicated. Right: view of the sealed structure from the back. The camera and the readout electronics are mounted on the backplate located at the focal point of the Fresnel lens.

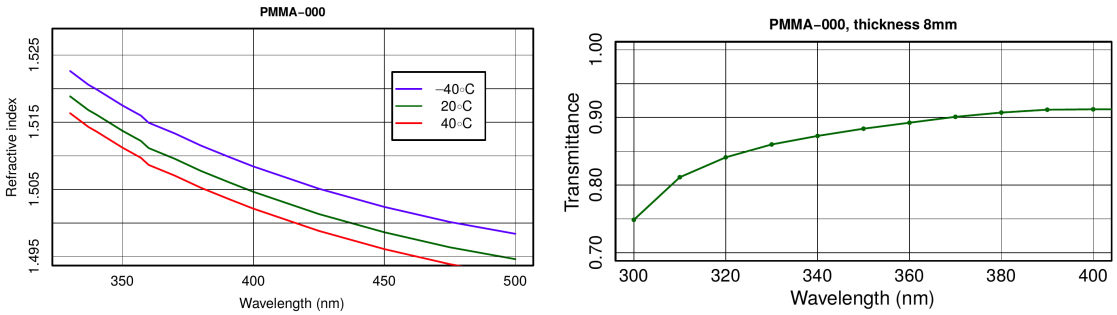

Figure 3. The Fresnel lens characteristics [29]. The plot on the left shows the refractive index in the near UV region for different temperatures from −40°C (top line) to 40°C (bottom line) and the plot on the right shows its transmittance as function of the wavelength.

space project to study ultra-high-energy cosmic rays by detecting the fluorescence light they produce when impinging on the atmosphere [20]. The main characteristics of the lens are shown in figure 3.

2.3 The mini-camera

The Cherenkov light focused by the lens is detected by the mini-camera, which is composed by the photo-detection plane, the electronic data acquisition system and the cooling system; the chain of electronic components in a single channel is represented in figure 4.

2.3.1 The photo-detection plane

The photo-detection plane of the mini-telescope, shown in figure 5-left, is made of 12 modules, each one hosting 12-pixels (see figure 5-right). Each pixel is a 23.2 mm flat-to-flat hexagonal light-guide coupled to a SiPM. The SiPM is a hexagonal large surface monolithic sensor of 93.56 mm^2 active area, divided into 4 channels with a common cathode. It is the first implemented SiPM with hexagonal shape and large dimensions, based on the Hamamatsu's Low Cross-talk Technology 2.

2020 JINST 15 P04004

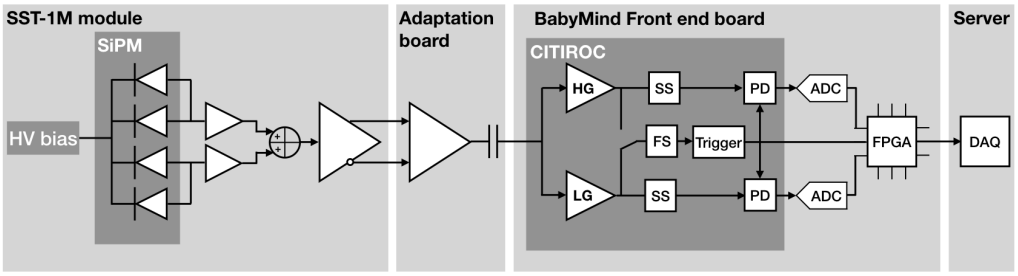

Figure 4. Simplified scheme of the readout electronics of a single camera channel. The SiPM has four channels, which are summed two by two and amplified. A differential amplifier provides a single DC coupled differential output. The adaptation board transforms the differential output to a single-ended output, reduces the gain and removes the DC component of the signal. Each SiPM is connected to a single CITIROC input. Inside the CITIROC ASIC, the signal is split into two paths: one variable gain pre-amplifier with a high gain (HG) and one with a low gain (LG). The user decides which of the two paths is used for the trigger and set a threshold. When the threshold is exceeded, a trigger signal is emitted and starts the peak detector (PD) for both HG and LG. Because it is important that when the trigger signal arrives to the peak detector the HG and LG signals did not yet reach their maximum, a slow shaper (SS) is used for the HG and LG paths while a fast shaper (FS) is used for the trigger paths. The trigger signal reaches the FPGA, which triggers the analogue to digital converters (ADC) that delivers a digital value for both HG and LG. The CITIROC control as well as data synchronisation and shipping to the data acquisition server are handled by the FPGA.

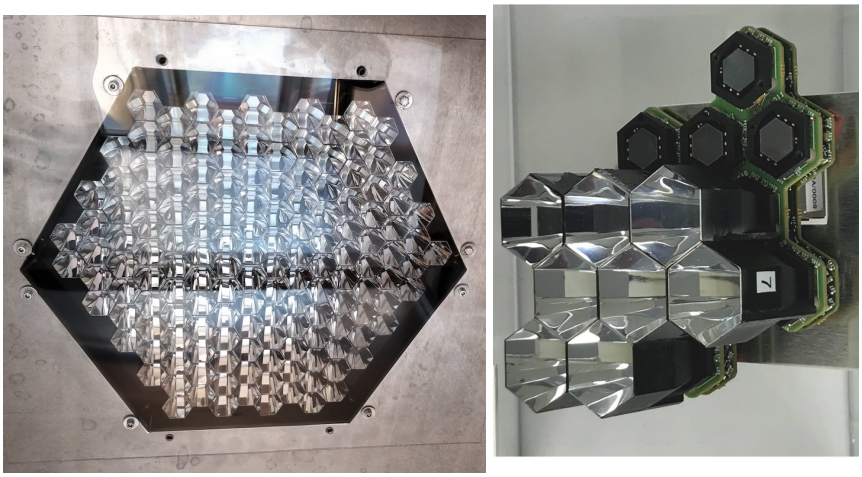

Figure 5. View of the photo-detection plane (left) and of one of the 12 modules with 12 pixels (right), where a reduced number of light guides and the SiPMs coupled to the preamplifier and slow control boards are visible.

The sensor is fully characterized in ref. [30]. Each channel is composed by a matrix of 9210 cells of 50 µm × 50 µm area.

Given its large surface area, the sensor has a large capacitance, which impacts the recovery time, and so the signal shape. To achieve the desired bandwidth, the preamplifier has been properly tuned to obtain signal duration of about 30 ns FWHM. The slow control board, described in ref. [24], feeds the preamplifier output signals in the readout electronics and also controls the bias voltage

2020 JINST 15 P04004

of the sensors, ensuring a real time correction of the bias voltage to compensate for changes of temperature. To this aim, the sensor package incorporates a negative temperature coefficient probe. The derived temperature value from the negative temperature coefficient is used by the slow control board to calculate the correction to apply to the bias voltage. This compensation loop allows to equalize the gain of the SiPM across the camera photo-detection plane, despite gradients of temperature across the plane may be present.

The light-guides, fully described in ref. [16], allow to suppress stray background light (light pollution, reflection on clouds, albedo, moonlight, etc., also called Night Sky Background or NSB), thus enhancing the signal to noise ratio and preventing optical cross-talk between pixels. Light-guides are industrially produced by injection molding of a poly-carbonate substrate of high optical quality, covered with an UV reflecting coating tuned for almost parallel incidence to surface [16].

Globally the mini-camera provides a total field of view of around 6.2°.

2.4 The readout electronics

The readout electronic boards have been designed by the electronics workshop of the Département de Physique Nucléaire. The FEB has in total 96 input channels which are connected with the preamplifier output of the photo-detection plane. As explained, the modules of the SST-1M camera were used without changing them. In these modules the 4 channels of each sensor are pre-amplified and summed. In a possible future configuration, a better strategy will be to read each of the 4 channels of each sensor with CITIROC directly. Nonetheless for this mini-camera, having adopted the existing modules, the preamplification of each channel is unavoidable. This is not optimal, especially for the high gain channel, because this limits its dynamic range (see section 3.1).

One part of the read-out system (see figure 4) is the CITIROC ASIC [25], whose main stages are:

- a *preamplification stage* comprising two gains to accommodate a larger dynamic range. The "High Gain" (HG) is used for small signals, i.e. produced by low-energy showers, while the "Low Gain" (LG) is for high-energy ones;
- a *charge measurement stage* for both HG and LG, using either a peak detector or a track and hold detector, preceded by a slow shaper and followed by a multiplexer. Signals from the 32 channels are multiplexed to a single analogue to digital converter (ADC) for digitization;
- a *trigger stage*, which can receive as input either the HG or the LG output signals. These are fed into a "fast shaper" with a peaking time of 15 ns. The signal is compared to a programmable threshold via 2 discriminators, one providing the trigger (OR32), also used for the hit register, and the other ($OR32_T$) providing the event time information of each channel.

The ASICs are controlled by a FPGA, which is the real core of the readout. Its essential role is to synchronize the charge and time data of each FEB, regulate the system (gain of the sensors, humidity, temperature, protection, etc.), manage memories, validate events, multiplex the inputs, as well as send out the data over the USB3 interface to the data acquisition server.

As shown in figure 6, at every clock cycle (2.5 ns), the trigger status of each of the channels is checked. If a trigger is found, the system is blind for 9.12 µs. This is the time needed to digitize the charge values of the 32 channels, therefore it introduces some dead-time. A reset signal is activated

2020 JINST 15 P04004

at the end of the process and the cycle can start again. This dead-time imposes to have a threshold high enough to minimize fake triggers, as for example the ones due to electronic noise, dark count of sensors and NSB. An additional threshold for both HG and LG is implemented on the charge output at the FPGA level. It provides an additional criterium and allows to discard events, even though they have been readout from the CITIROC ASIC. The BabyMind architecture has been slightly modified for the purpose of this project such that one single channel above threshold can force the acquisition of the charge for all other channels. Therefore, for each triggered event, the information of all pixels is available and can be used for the shower image analysis.

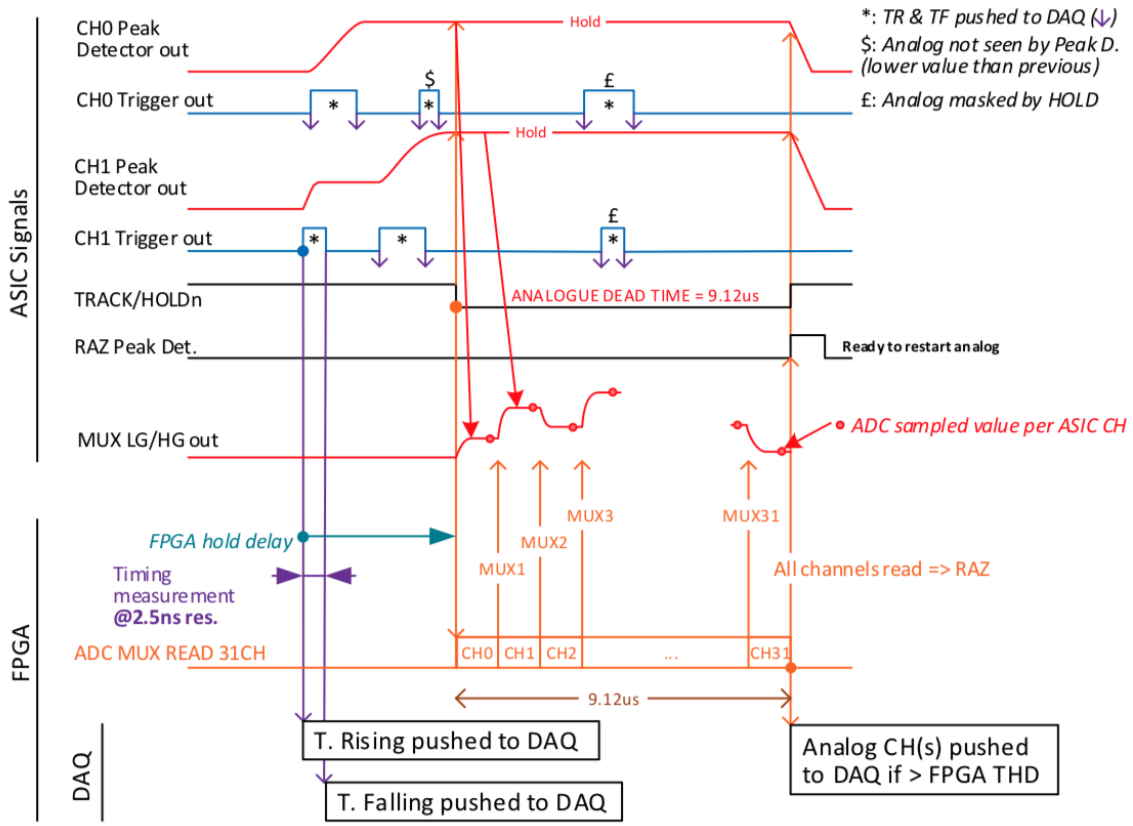

Figure 6. Time and analog sampling of the Front End Board.

2.4.1 The cooling system

The front-end electronics needs a power of about 0.35 W per channel, and the mini-camera has to be cooled to keep the photo-detection plane in reasonable working conditions (20°C–30°C, depending also on the external temperature). Since the mini-camera is not operated in a sealed environment where the humidity level can be controlled to avoid condensation, the cooling is realized with 16 fans mounted in "push-pull" configuration (see figure 7-left). The small gap between the boards and the mounting plate limits the air flow, causing a temperature gradient across the photo-detection plane of about 10°C, when measured at room temperature in the laboratory (see figure 7-left). Though not optimal, this temperature gradient is acceptable for the requirements of this small project, since

2020 JINST 15 P04004

the slow control board further equalizes the gains across pixels. The camera is protected by a non-coated 2 mm thick Poly (methyl methacrylate) window which also helps in channeling the air across the photo-detection plane for the cooling.

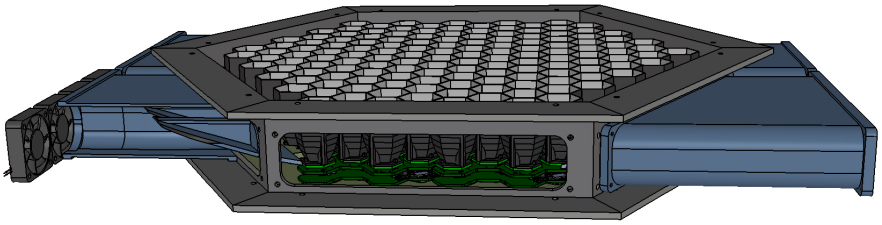

Figure 7. CAD of the photo-detection plane with the cooling system based on a push-pull principle. The fans are mounted on 3D-printed blocks that channel the air between the two printed circuit boards of the optical modules.

3 The mini-camera calibration

The goal of the calibration is to extract for both HG and LG channels (see section 2.4) the correspondence between ADC counts and p.e.s in the dark and for different NSB levels. With a full simulation of the telescope, which is beyond the scope of this work, this relationship could be brought further to relate the number of p.e.s to the primary particle. For our system, the ADC-p.e. correspondence is far from trivial. As a matter of fact, the SiPM signals are preamplified before being fed to CITIROC, which affects the single photon resolution.

Moreover, the absence of an external trigger makes the single photon calibration or the acquisition of a multiple p.e. spectrum very complicated as the probability to actually acquire the data when the LED flashing rate is very low. Without the multiple p.e. spectrum the gain cannot be determined precisely. For any acquisition, the trigger threshold should be high enough to avoid that the ASIC constantly processes background data and therefore runs at high dead-time probability. As a matter of fact, the typical dark count rate of the hexagonal SiPM is 3 MHz, which is more than one order of magnitude higher than the readout capabilities of the present readout system ($\lesssim$ 100 kHz with deadtime). For instance, if ones needs to perform dark count runs, the threshold should be set higher than the electronic noise level. Similarly, if few photons are injected with an external light source, the threshold must be set higher than the single-photon amplitude to avoid contributions from dark photons. Also, during observations, the threshold has to be set in order to discard most of the NSB induced triggers (see section 3.2).

Eventually, it should also be noted that background light affects the correspondence between ADC count and p.e. due to the "voltage drop" effect explained in section 3.2 (see also [31]). Hence, we performed a calibration of the response of the mini-camera for different light background conditions to emulate different NSB p.e. rates.

2020 JINST 15 P04004

In the next sections, we first focus on the correspondence between the CITIROC ADC counts (both for HG and LG) and number of p.e. in dark conditions (see section 3.1) and then with emulated NSB (see section 3.2).

3.1 Calibration of the ADC count-number of p.e. in the dark

The calibration has been performed using a single LED driven by a pulse generator at different voltages, i.e. light intensities. The first step consists in connecting the SST-1M module directly to an oscilloscope. The single p.e. amplitude is derived from a measurement in the dark. The light intensity in p.e. for various LED voltages is then derived by dividing the measured average amplitude by the single p.e. amplitude. Once the correspondence between LED voltage and light amplitude is determined, the module is connected to the CITIROC boards and is illuminated with the LED using the same pulse levels used for the p.e. calibration. The result of the measurements with CITIROC are shown in figure 8, for both HG and LG, together with the linear fit results. The two curves start at 6 p.e., which is the trigger threshold used to prevent high trigger rate from dark noise events. The LG has an acceptable response, while the HG is linear only up to a few p.e. . The HG channel as a trigger source is practically not usable above 400 MHz of NSB and this is why observations on field use the LG trigger. We can also notice that the LG has linear behavior up to about 750 p.e., which we consider the upper limit of the dynamic range. For higher light intensities, the preamplification stage of the adopted SST-1M module saturates and affects the amplitude of the pulse. In the SST-1M camera, when the saturation occurs, the number of p.e. can still be derived from the integral of the pulse with marginal losses in resolution [15]. This functionality could be in principle achieved with the CITIROC ASIC using the time-over-threshold information, but at this stage the readout cannot cope with the timing information of all the camera channels. This problem needs further investigation and a new iteration of the FEB design to be solved.

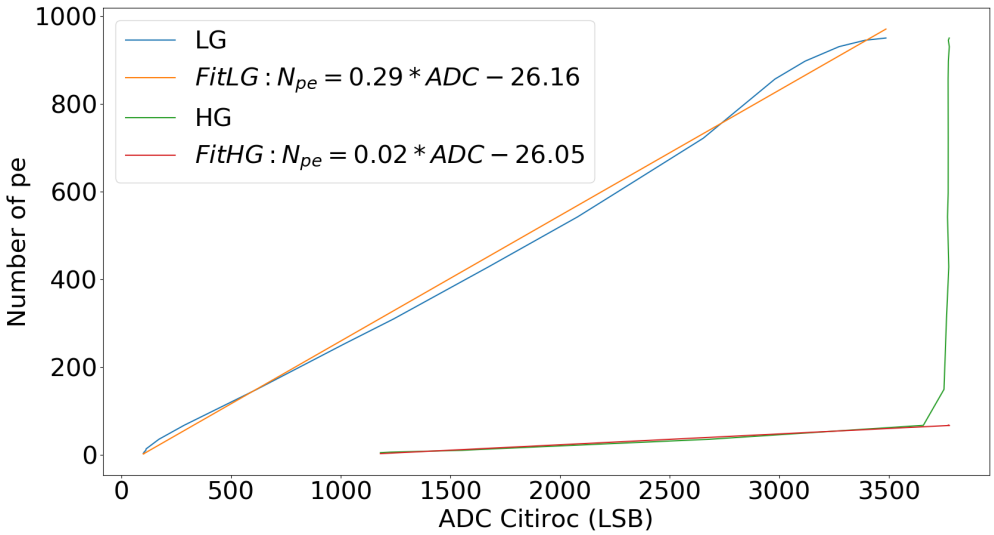

Figure 8. Number of p.e. vs. CITIROC ADC count expressed in terms of least significant bit (LSB) for HG and LG and corresponding fits.

2020 JINST 15 P04004

3.2 AC-DC scan for various emulated NSB levels

The Camera Test Setup (CTS) built for the calibration of the SST-1M camera was used [15] to evaluate the mini-camera performance at different NSB levels. The CTS allows to emulate the flashes of Cherenkov light from atmospheric showers and the continuous level of NSB, simultaneously. This is done by means of two LEDs facing each pixel, one operated in pulsed mode (AC) and another one in steady current mode (DC). The intensity of each type of LED can be adjusted by mean of a digital to analog converter (DAC). The CTS has been previously calibrated with the SST-1M camera and the emulated NSB p.e. rates as a function of the DAC DC values are shown in table 2. It should be mentioned that only one DAC value can be set for a group of 48 DC LEDs. The assembly procedure of the boards together with the electronics components tolerances cannot ensure that all LEDs will respond identically to a given DAC value. A NSB spread of about 10% was measured between the 48 pixels at a given DAC value and this error applies to the NSB frequency in table 2.

Table 2. Conversion from DAC DC value to frequency of NSB in MHz for a typical CTS pixel.

CTS DAC DC values	200	240	250	300	330	350	380	400	450
NSB frequency (MHz)	10	20	25	100	400	800	1700	2000	2300

To get the ADC values of CITIROC as a function of the signal emulated by the CTS in terms of the DAC AC value, we perform a so called AC-DC scan for all the pixels of the camera. The CITIROC is readout, while flashing on the sensor with different LED light intensities (DAC AC) and while different continuous NSB levels (DAC DC) are also emulated. Results are shown in figure 9 for the LG channel of one typical pixel.

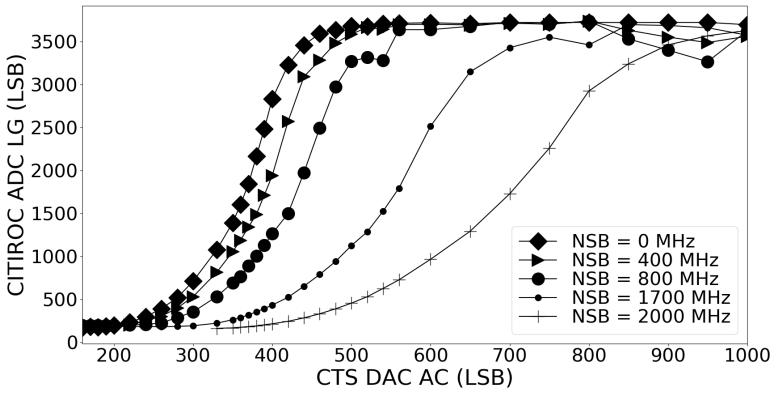

Figure 9. AC-DC scan results for the amplitude of the signal measured in the LG channel of one pixel for different emulated NSB levels.

Figure 9 demonstrates that for increasing NSB intensities, more light (higher DAC AC value) is needed in order to get the same amplitude as in dark conditions. This is due to the gain drop, induced by the "voltage drop" effect, which affects the signal amplitude. As matter of fact, a constant light level produces a steady current flowing through the sensor and also through the polarization resistor that is usually put in series with it to protect it. This resistor causes a voltage drop that reduces the

2020 JINST 15 P04004

bias voltage of the sensor and hence its PDE, gain and optical cross talk. More details about this effect can be found in [32]. So signals with the same amount of photons appear as weaker because of the NSB. The resulting overall amplitude drop can be estimated from figure 9 by calculating the ratio between the average detected amplitude with a given NSB level and the one acquired in dark conditions. The result is shown in figure 10 and can be used to derive the number of impinging photons for a given detected signal provided that the NSB intensity is known.

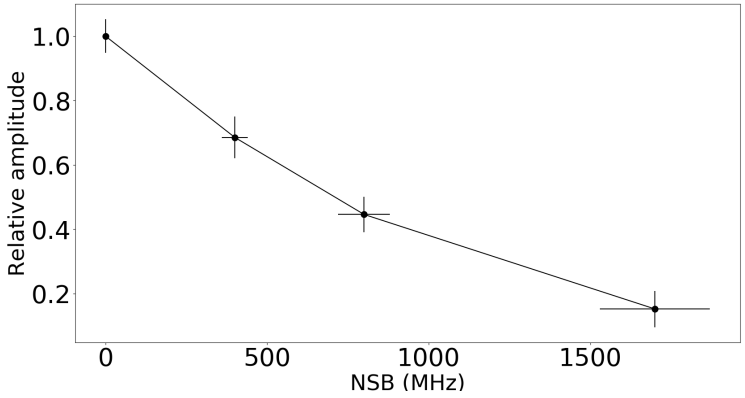

Figure 10. Relative amplitude loss (including gain, PDE and optical cross talk drop) as a function of the NSB induced p.e. rate.

Currently, it is not possible during observations with the mini-camera to establish the exact value of the NSB rate. While the SST-1M readout is DC coupled and therefore the baseline shift can be used to derive the NSB level, the mini-camera readout is AC coupled and without dedicated instrumentation, the NSB level cannot be extracted. Therefore, in the following sections, only ADC count units are preferred with respect to p.e. for the CITIROC output. For future observation campaigns, a dedicated device will be used for NSB monitoring and for determination of number of p.e. corresponding to different NSB levels. It will consist of a single pixel, identical to the one of the camera, located at the edge of the camera but biased by an external voltage source of which the current can be monitored in real time.

4 Results of the observation campaigns

We have performed two observing campaigns at the Observatory of Sauverny and at the astronomical observatory of OFXB[1] at Saint-Luc, Switzerland, on July 2019. Both sites present non negligible level of NSB due to the vicinity of Geneva city center (Sauverny) or presence of clouds and Moon (Sauverny and St Luc), which is changing over night. Therefore, the trigger threshold must be set such that atmospheric shower events are favored compared to NSB induced triggered events. To do so, trigger scans are performed before each run.

In figure 11, the results of a typical trigger rate scan performed during the observation night at Sauverny with the HG channel connected to the fast shaper are shown. Similarly, figure 12 is

[1] http://www.ofxb.ch.

2020 JINST 15 P04004

obtained with the LG channel connected to the fast shaper. One can see from these two figures that with the LG channel the threshold can be set when the steep slope dominated by NSB hardens into a flatter line (which we call 'plateau'), above a DAC threshold of 270. In this region, mostly atmospheric showers and also muons, are detected. However with the HG channel, this plateau is never reached and therefore the threshold cannot be set at a value that would suppress NSB induced triggers. Therefore, for these observation, the LG was selected as input for the trigger path. In figure 11, we compare the results of the trigger rate scans measured in Sauverny to the ones measured with the CTS in the laboratory. This allows to estimate that the NSB measured in Sauverny ranges from 800 MHz and 2 GHz, which is in good agreement with the rough estrapolation from SST-1M values performed in section B and presented in table 3.

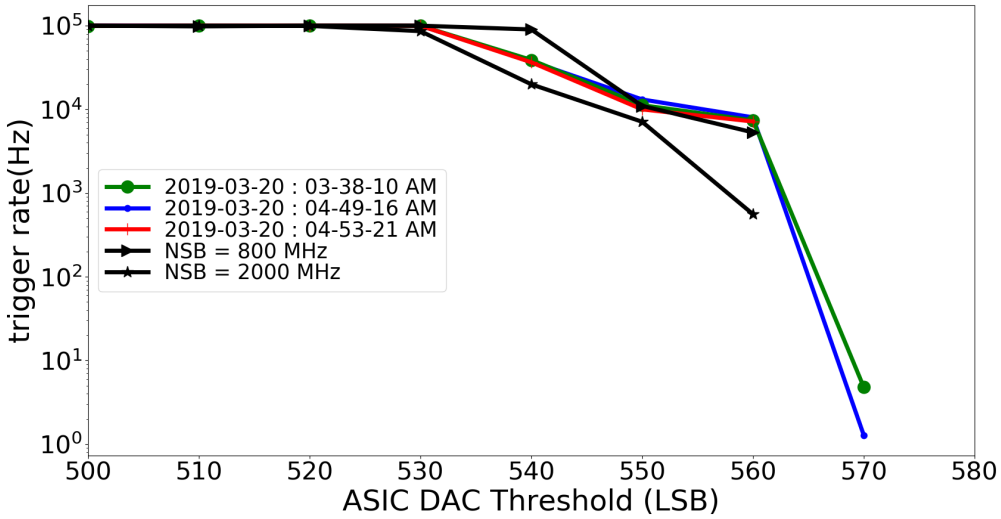

Figure 11. Trigger rate scans obtained using the HG trigger path at different times of the night and different elevations in Sauverny. These curves are compared to the ones obtained in the laboratory with the CTS.

In figure 12, different trigger rates, ranging from 0.02 Hz to 1 Hz were recorded above LSB ~ 270. This variation can be explained by the different zenith angles of the telescope and underlying NSB contribution at which the data were acquired. The measured rates are above the estimate made in section B. This is expected since eq. (B.6) does not include the contribution of muons, which interact directly into the photosensors or with the surrounding material [33]. An example of two atmospheric showers acquired in Sauverny are shown in figure 13.

The absence of bright cities in the vicinity and the altitude of 2200 m make the observatory in Saint-Luc a far better observation site than Sauverny.

Figure 14 displays the result of the trigger rate scans for the LG channel at different night times and different zenith angles. Despite the better sky quality, the presence of the moon during the night of observation in Saint-Luc explains why the obtained trigger rate scan is not too far from the one shown in figure 12. As already observed, the observed trigger rates above LSB of 270 are in the range 0.2–1 Hz. This plateau is reached a bit earlier than in Sauverny, indicating the possibility to have a lower energy threshold thanks to the lower NSB.

2020 JINST 15 P04004

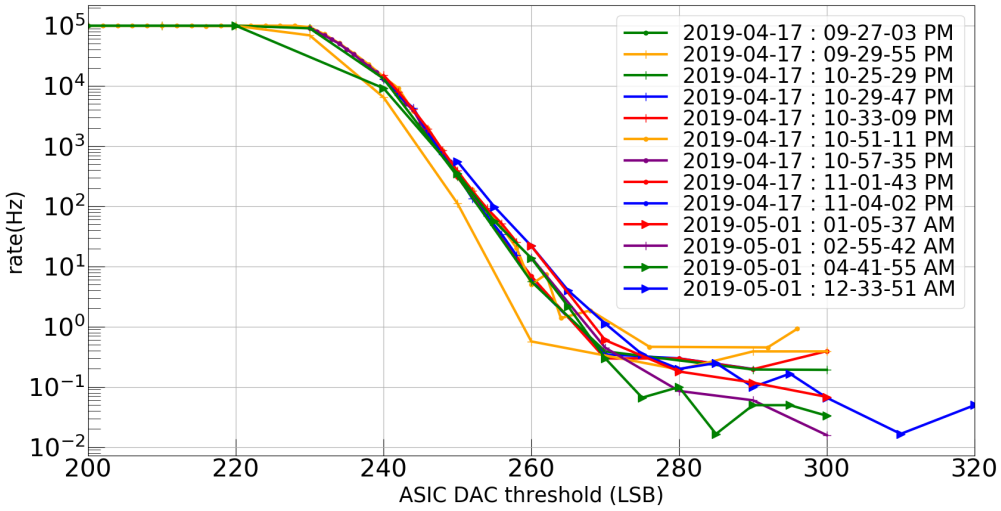

Figure 12. Trigger rate scans obtained using the LG trigger path at different times and elevation in Sauverny.

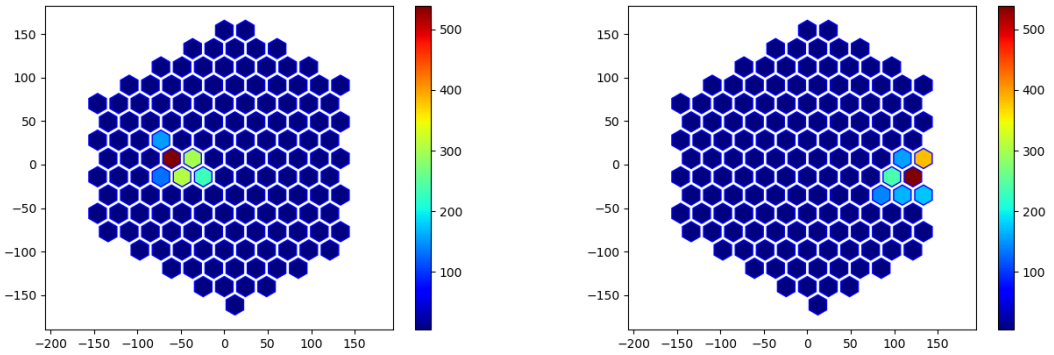

Figure 13. Examples of observed shower events at the Observatory of Geneva in Sauverny.

In figure 15 the three variables accessible for each pixel of the camera are shown for a typical atmospheric shower. Figure 15-left shows the time at which the signal passed the trigger threshold inside the FPGA clock window of 2.5 ns. The development of the shower image from the edge to the center of the camera is then clearly visible. Figure 15-center shows that the HG channel cannot be used for image reconstruction as except for one pixel it is saturated. However, the LG channel visible on figure 15-right remains below saturation and allows to identify the shower image structure.

4.1 The mini-telescope effective area

The effective area should be derived using Monte Carlo simulations of the physics process and the detector, processed through a similar analysis chain than that applied to data. Nonetheless, a full simulation work is beyond the scope of this paper, since for the moment we plan only to use

2020 JINST 15 P04004

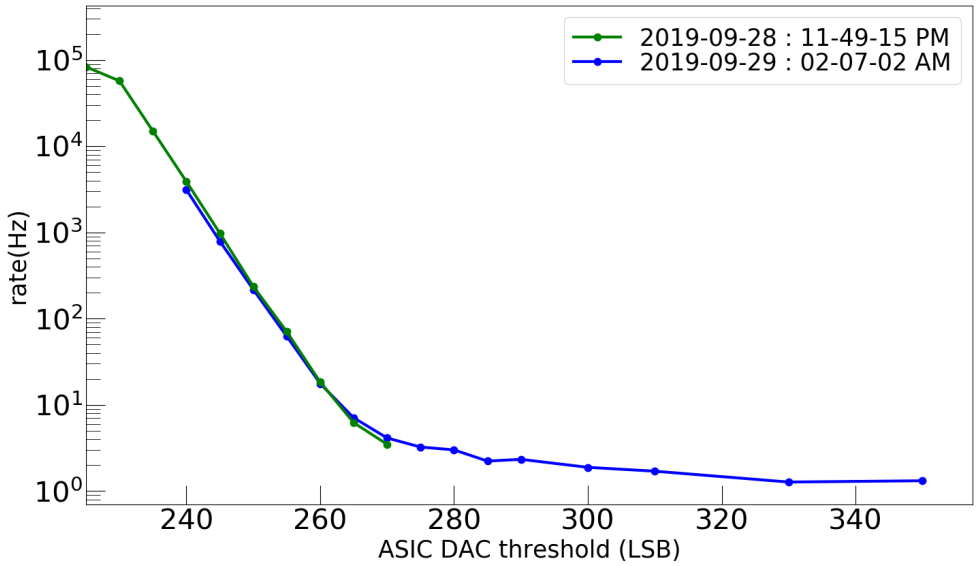

Figure 14. Trigger rate as a function of the low gain threshold at the Saint-Luc observatory for two different scans during the night. For higher threshold values, the acquisition time for each threshold has been increased from five seconds to two minutes in order to accumulate more statistics.

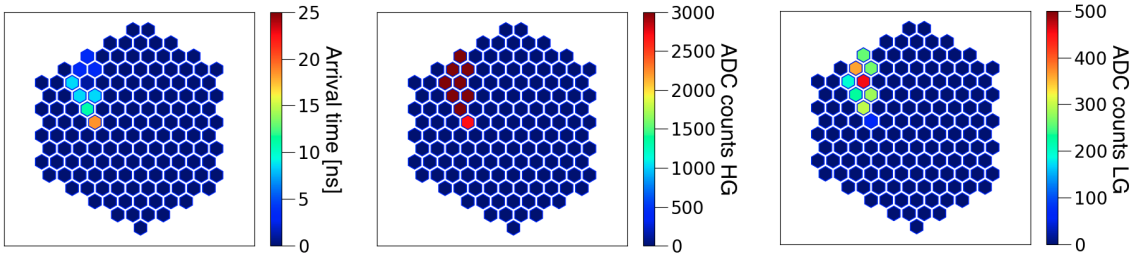

Figure 15. Timing (in ns) of pixels hit by a shower event (left) and its LG (center) and HG (right).

the mini-telescope for outreach and to better understand the behaviour of CITIROC. Moreover, Fresnel lenses were only introduced very recently in the framework that could have been used, the sim_telarray package [34], and they are still in validation phase. In addition, no full image data analysis pipeline is implemented. Consequently, for the purpose of this paper the effective area is computed analytically, assuming the relationship: $E = E_0\, C^{\alpha}$ between the detected charge C in the camera and the true primary energy E, while E_0 is a constant. As already done before, we assume that the true cosmic-ray flux is given by eq. (B.5). Hence, the differential effective area is:

$$dS = \frac{dN/dt}{dE\ d\Omega} * \frac{1}{I} = \frac{dR/d\log C}{\alpha\, E_0^{-1.7}\, d\Omega} \times \frac{1}{1.8 * 10^4 C^{-1.7\alpha}}\,. \tag{4.1}$$

In eq. (4.1), $\frac{dR}{d\log C}$ is the differential trigger rate as a function of the logarithm of the image total charge, as shown in figure 16. In this figure, we observe the clear separation between noise and

2020 JINST 15 P04004

signal at total LG charge in an image of ~ 200 ADC counts. Given that the cumulative rate above the total charge of 200 ADC counts is 2 Hz, using eq. (B.6), we see that this value corresponds to a cosmic-ray threshold of 6 TeV. Therefore, the effective area will only be evaluated above 200 ADC counts. i.e. 6 TeV. Moreover, we consider that $E_0 = \frac{6\,\mathrm{TeV}}{200^{\alpha}}$.

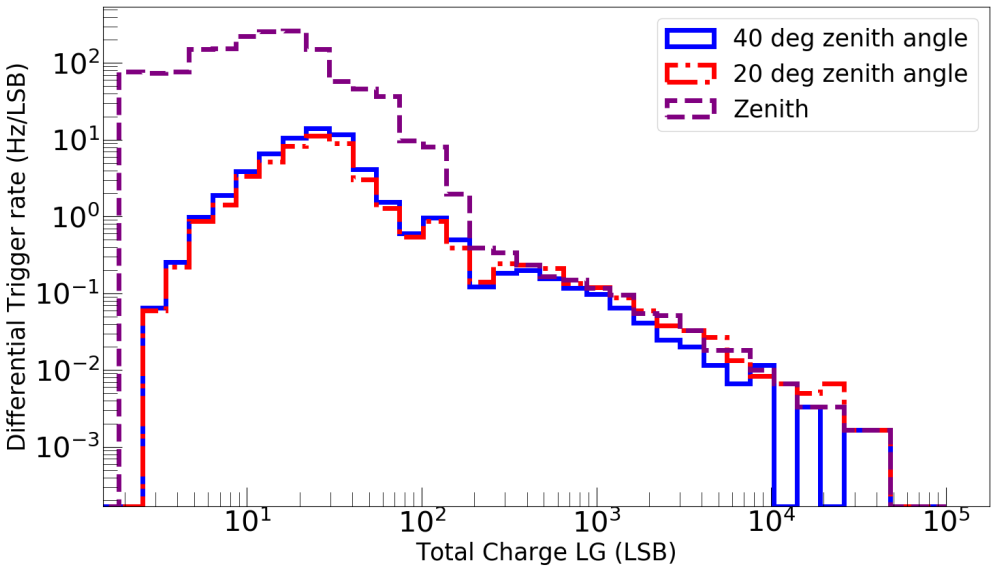

Figure 16. Differential trigrate as a function of the ADC low gain total charge (in log scale) at the Saint-Luc observatory for different zenith angles.

It remains to determine α. By observing figure 19–left, the density of Cherenkov photons as a function of the primary energy follows a power law $D_{\mathrm{ch}} \simeq 81.28\,E^{1.14}$. If we make the reasonable assumption that the detected charge in the camera increases linearly when the photon density increases, then $D_{\mathrm{ch}} \propto C \Rightarrow E \propto C^{1/1.14} \propto C^{0.87}$, hence $\alpha = 0.87$. As a matter of fact, we know that the acquisition system is linear up to 750 p.e. in dark conditions, as shown in figure 8. Hence, the energy $E = E_0\,C^{0.87}$ and $E_0 \sim 0.06$ TeV. For these values, figure 17 shows the effective area according to eq. (4.1). A good indication that the derived effective area based on simple approximation is a good estimate of the real one is that the inflexion point is observed around 5×10^4 m^2, which corresponds to the area of a disk of radius 130 m. This is roughly the expected radius of Cherenkov light pools at ~2000 m altitude in this energy range [35].

5 Conclusions and outlook

In this work, we showed that a mini-telescope, built with 144 SiPM pixels and their readout electronics coupled to the CITIROC ASICs, provides sufficient performance to detect gamma-rays and cosmic rays with energy above some tens of TeV. We showed that measured rates are compatible with analytic estimates. A charge calibration has been done as a function of different NSB levels. In order to translate measured charge into number of photons hitting the camera, further work and an external device to measure the NSB would be needed.

2020 JINST 15 P04004

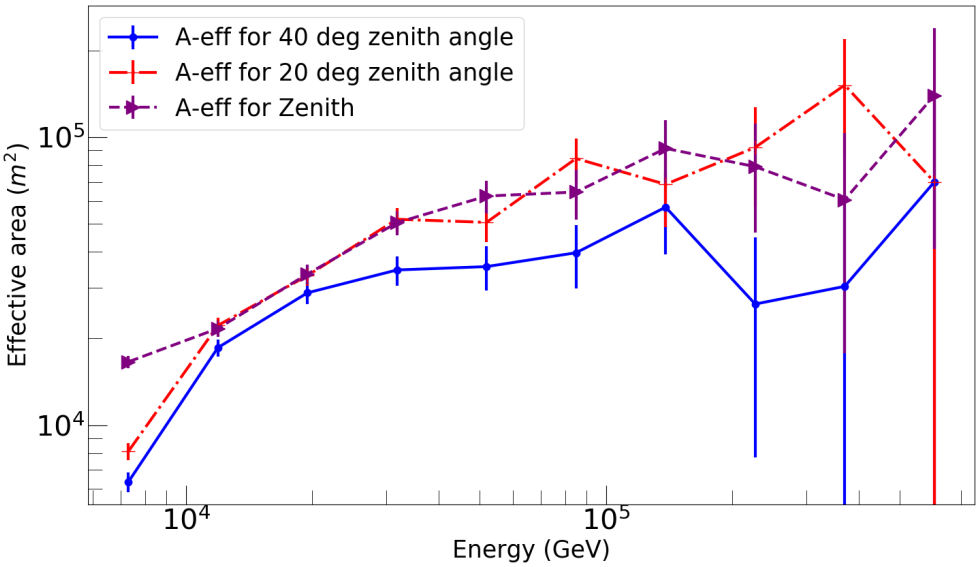

Figure 17. Effective area of the mini-telescope as a function of the energy of gamma-rays at the Saint-Luc observatory for different zenith angles.

Such a study shows that an array of such cost effective mini-telescopes (~ 20 k€) could be used to complement other shower detectors, such as larger and more expensive IACTs or water Cherenkov ponds, which have better sensitivity and lower threshold. An array of such a small telescopes, operated in stereo mode, would improve gamma/hadron separation of a water pond or larger telescopes thanks to their imaging capability. It would also provide an independent measurement of the shower direction and energy. In stereo mode, both trigger and energy threshold can be lowered with respect to the single telescope case illustrated in this paper.

Acknowledgments

This project is the result of a collaboration between the Multi-Messenger High-Energy Astrophysics group of the Département de Physique Nucleaire et Corpusculaire (DPNC), the Department of Astronomy and the Department of Computer Sciences at the University of Geneva. We thank the BabyMind DPNC colleagues, in particular E. Noah for providing the FEBs. We thank the Swiss Confederation since S. Njoh Ekoume was supported by the Program "Boursier d'excellence" [36]. Mechanical and electronics workshop, both at the University of Geneva Observatory in Sauverny and at the Observatory of Saint-Luc.

2020 JINST 15 P04004

A Analytic development of electromagnetic showers

A simplified model of analytic development of the electromagnetic shower, called the "Heitler model" [1, 37], will be used to estimate figure 19-left. We consider that:

- The primary particle is a gamma-ray.
- The involved processes are only production of electron-positron pairs, and bremsstrahlung. It is assumed that their typical interaction lengths are the same. Actually, the average distance for pair production is $\lambda_{\text{pair}} \sim \frac{9}{7} X_0 \Rightarrow \lambda_{\text{pair}} \simeq 48.6\,\text{g}\cdot\text{cm}^{-2}$. The radiation length is the average distance beyond which a high-energy electron looses 1/e of its energy by bremsstrahlung [38]:

$$X_0 = \frac{716.4 \cdot A}{Z(Z+1)\ln(287/\sqrt{Z})} \quad [\text{g}\cdot\text{cm}^{-2}] \tag{A.1}$$

  where A and Z are the equivalent atomic number and mass number of the atmosphere. For the atmosphere, $X_0 \sim 37.8\,\text{g}\cdot\text{cm}^{-2}$.
- Photons and electrons in the same atmosphere layer share the same energy in equal amounts.
- The production of particle process stops below the critical energy, and after ionisation losses dominate.

The profile of showers resulting from these hypotheses is represented in figure 18, where we can discern steps in radiation length and the number of photons and charged particles produced at each step. In the first step, a gamma-ray produces an electron-positron pair, and the charged particles radiate in the next step. The multiplication process stops for charged particle energies lower than the critical energy, which in the atmosphere is [38]:

$$E_{\text{crit}}^{\text{atm}}\,(\text{MeV}) = \frac{710}{Z + 0.92} \Rightarrow E_{\text{crit}}^{\text{atm}} \simeq 80\,\text{MeV} \tag{A.2}$$

Considering figure 18, we can establish a mathematical model describing the number of charged particles and photons at each radiation length step n:

$$n_{\text{ph}(n)} = n_{e(n-1)} \tag{A.3a}$$

$$n_{e(n)} = n_{\text{ph}(n-1)} \cdot 2 + n_{e(n-1)} = 2n_{\text{ph}(n-1)} + n_{\text{ph}(n)} \tag{A.3b}$$

where $n_{\text{e}(n)}$ ($n_{\text{e}(n-1)}$) and $n_{\text{ph}(n)}$ $n_{\text{ph}(n-1)}$ represent the number of charged particles and the number of photons sfter n (n-1) radiation lengths steps, respectively. Equations (A.3a) and (A.3b) imply:

$$n_{\text{ph}(n+1)} = n_{\text{e}(n)} \Rightarrow n_{\text{ph}(n+1)} = n_{\text{ph}(n-1)} \cdot 2 + n_{\text{ph}(n)} \tag{A.4}$$

Consequently, we define:

$$D_n = n_{\text{ph}(n-1)} + n_{\text{ph}(n)} \tag{A.5a}$$

$$S_n = n_{\text{ph}(n)} - 2 \cdot n_{\text{ph}(n-1)} \tag{A.5b}$$

2020 JINST 15 P04004

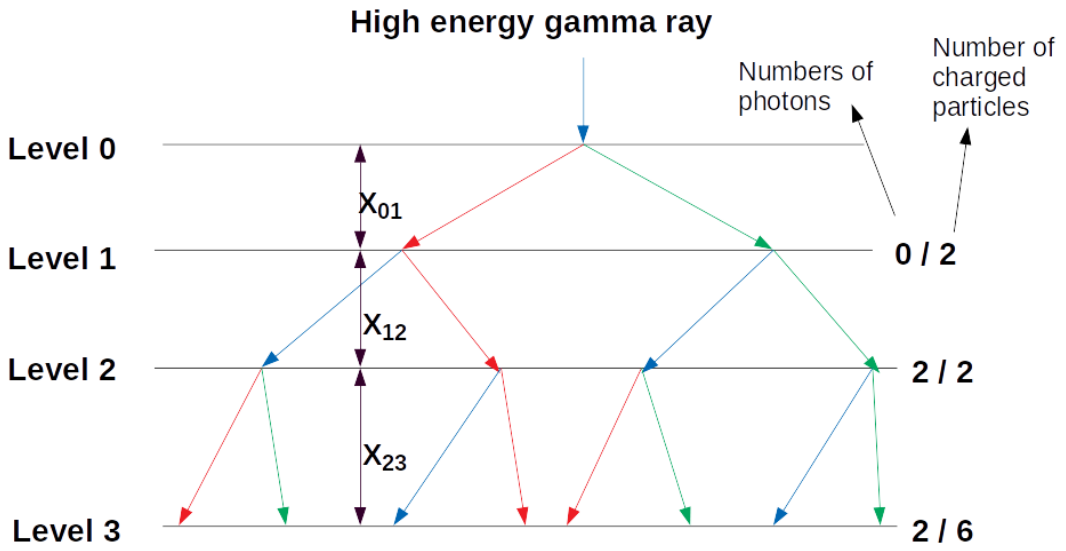

Figure 18. Illustration of the Heitler's toy model of an electromagnetic shower. Photons are represented in blue, electrons in red and positrons in green. The radiation length is assumed equal to the pair production interaction length. The number of photons and charged electrons is indicated.

From the above equations, we deduce $2 \cdot D_n + S_n = 3 \cdot n_{\mathrm{ph}(n)}$. And we can further develop the above eq. (A.5a) and e.g. (A.5b):

$$D_n = n_{\mathrm{ph}(n-1)} + n_{\mathrm{ph}(n)} \Rightarrow D_{n+1} = n_{\mathrm{ph}(n+1)} + n_{\mathrm{ph}(n)} \tag{A.6a}$$

$$\Rightarrow D_{n+1} = n_{\mathrm{ph}(n-1)} \cdot 2 + n_{\mathrm{ph}(n)} + n_{\mathrm{ph}(n)} \Rightarrow D_{n+1} = 2 \cdot (n_{\mathrm{ph}(n-1)} + n_{\mathrm{ph}(n)}) \tag{A.6b}$$

$$\Rightarrow D_{n+1} = 2 \cdot D_n \Rightarrow D_n = 2^{n-1} \tag{A.6c}$$

$$S_n = n_{\mathrm{ph}(n)} - 2 \cdot n_{\mathrm{ph}(n-1)} \Rightarrow S_{n+1} = n_{\mathrm{ph}(n+1)} - 2 \cdot n_{\mathrm{ph}(n)} \tag{A.6d}$$

$$\Rightarrow S_{n+1} = n_{\mathrm{ph}(n-1)} \cdot 2 + n_{\mathrm{ph}(n)} - 2 \cdot n_{\mathrm{ph}(n)} \Rightarrow S_{n+1} = n_{\mathrm{ph}(n-1)} \cdot 2 - n_{\mathrm{ph}(n)} \tag{A.6e}$$

$$\Rightarrow S_{n+1} = -S_n \Rightarrow S_n = -2 \cdot (-1)^{n-1} \Rightarrow S_n = -2 \cdot (-1)^{n-1} \cdot (-1)^2 \tag{A.6f}$$

$$\Rightarrow S_n = -2 \cdot (-1)^{n+1} \tag{A.6g}$$

From (A.6c) and (A.6g), we obtain:

$$n_{\mathrm{ph}(n)} = \frac{2}{3} \cdot [2^{n-1} - (-1)^{n+1}] \tag{A.7}$$

From (A.3a), $n_{\mathrm{e}(n)} = n_{\mathrm{ph}(n+1)}$, so that this result combined with (A.7) gives:

$$n_{\mathrm{e}(n)} = \frac{2}{3} \cdot [2^n - (-1)^n] \tag{A.8}$$

The number of charged particles after n radiation lengths is therefore:

$$n_{\mathrm{e}(n)}^{\mathrm{total}} \simeq \frac{4}{3} \left(2^{n-1} - \frac{(-1)^n}{2} \right) \tag{A.9}$$

2020 JINST 15 P04004

A.1 Total distance traveled by shower charged particles

The total length traveled by all charged particles in an atmospheric shower is needed in order to estimate the density of Cherenkov photons produced by a shower at ground. This is expressed by the relation:

$$T_{\text{tot}} = \sum_{n=1}^{n_{\max}} (n_{e(n)} \cdot (L_n - L_{n-1})) \tag{A.10}$$

where L_n is the distance from the sea level to the level n. L_0 is the distance from the sea level to the level of the first interaction of the primary particle.

In order to calculate L_n, we consider the simplified differential equation of pressure variation with respect to altitude z:

$$\frac{dP}{dz} = -\rho(z)g \tag{A.11}$$

From the perfect gas law, we can deduce (A.12) where n the number of moles, m is the mass of the gas atoms, $M = 28.966 \cdot 10^{-3}\,\text{kg mol}^{-1}$ is the molar mass for the atmosphere, $R = 8.31451\,\text{J mol}^{-1}\,\text{K}^{-1}$ the universal gas constant, and T is the temperature:

$$\begin{aligned} PV = nRT \Rightarrow PV = \frac{m}{M}RT \Rightarrow \frac{m}{V} = P\frac{M}{RT} \\ \Rightarrow \rho(z) = P\frac{M}{RT(z)} \Rightarrow \frac{dp}{dz} = \frac{PM \cdot g}{RT(z)} \end{aligned} \tag{A.12}$$

We can identify two regions with different temperature variations with altitude:

- Between 11–20 km the isothermal approximation applies since the temperature is about constant and equal to 216.5°K. By solving eq. (A.12), we get:

$$P(z) = P_{z=11'000\,\text{m}} \cdot e^{-\frac{M \cdot g}{RT}(z-11'000)} \tag{A.13}$$

  where $P_{z=11'100\,\text{m}} = 2.2637712 \cdot 10^4\,\text{Pa}$ is the pressure at 11 km. We then calculate the atmospheric depth in g/cm^2 starting from 11 km from the relation: $X(z)\,[\text{g/cm}^2] = \text{P(z)/g} \sim 10^{-2}\,\text{P(z)}\,[\text{Pa}]$, where we approximated the gravity acceleration $g = 9.8 \sim 10\,\text{m/s}^2$. From eq. (A.13), we calculate the altitude (in m):

$$z = \frac{RT}{Mg} \cdot \ln\left(\frac{P_{z=11\,\text{km}} \cdot 10^{-2}\,(\text{kg/N})}{nX_0}\right) + 11'000 \tag{A.14}$$

  where we considered that in the atmospheric depth $X(z)$ there are n radiation lengths. Hence, the first interaction point altitude is given by the above equation for $n = 1$ and its value is: $L_0 \simeq 22\,\text{km}$. In general, for n radiation lengths (in m):

$$\Rightarrow L_n = \frac{RT}{Mg} \cdot \ln\left(\frac{P_{z=11\,\text{km}} \cdot 10^{-2}(\text{kg/N})}{n \cdot X_0}\right) + 11'000 \tag{A.15}$$

- Between 0 and 11 km, the temperature varies linearly with altitude and the temperature gradient is constant and equal to $a = 6.5 \cdot 10^{-3}\,\text{km}^{-1}$. Hence, $T(z) = T_0 - a \cdot z$ and using this

2020 JINST 15 P04004

formula in eq. (A.12), we obtain:

$$\Rightarrow X(z) = P_1 \cdot 10^{-2}\,(\mathrm{kg/N}) \cdot \left[1 - \frac{a}{T_1} \cdot (z - z_1)\right]^{\frac{Mg}{Ra}} \tag{A.16}$$

$$\Rightarrow L_n = \left[1 - \left(\frac{n \cdot X_0}{P_1 \cdot 10^{-2}\,(\mathrm{kg/N})}\right)^{Ra/Mg}\right] \cdot \frac{T_1}{a} + Z_1 \tag{A.17}$$

where P_1, Z_1 and T_1 are respectively the pressure, the altitude above sea level and the temperature at the observation site and at the time of observations.

A.1.1 Characteristics of Cherenkov light emission

The area of the Cherenkov radiation cone produced by the shower when it intercepts the ground can be defined by the relation:

$$\mathrm{Area} = \pi \cdot \left[(L_0 - Z_1)\mathrm{tg}\left[\cos^{-1}\left(\frac{1}{\beta \cdot n_i}\right)\right]\right]^2 \tag{A.18}$$

where Z_1 is defined above.

The refractive index in the atmosphere n_i varies according to the temperature, the wavelength, and even the pressure. We ignore the variation with the wavelength, but still consider the dependency on the temperature and pressure:

$$n_i(L_n) = 1 + n_i(Z_1) \cdot e^{-L_n/h_0} \tag{A.19}$$

where $n_i(Z_1) = 1.00029$ is the value of the refractive index for instance at Sauverny and $h_0 = 7.1\,\mathrm{km}$.

The number of Cherenkov photons from charged particles of an electromagnetic shower per unit length and wavelength λ, emitted by a charged particle Ze and velocity $v = \beta c$ is given by:

$$\frac{d^2N}{dx \cdot d\lambda} = \frac{2\pi\alpha z^2}{\lambda^2}\left(1 - \frac{1}{\beta^2 \cdot n_i^2}\right) \tag{A.20}$$

where α is the fine structure constant and, as already noted, we ignore the dependency of n_i from λ. Integrating over the wavelength region where the Cherenkov spectrum is relevant (from $\lambda_1 = 300\,\mathrm{nm}$ to $\lambda_2 = 700\,\mathrm{nm}$), we obtain the relation:

$$\frac{dN}{dx} = 2\pi\alpha z^2 \sin^2(\theta)_{\mathrm{ch}} \int_{\lambda_1}^{\lambda_2} \frac{d\lambda}{\lambda^2} \Rightarrow \frac{dN}{dx} = 873.13 z^2 \sin^2(\theta)_{\mathrm{ch}}\,\mathrm{photons/cm} \tag{A.21}$$

All these formulas were compiled in a python script, to obtain figure 19-left, which represents the density of Cherenkov photons at ground as a function of the gamma-ray primary energy.

B Estimate of the physics reach of the mini-telescope

The evaluation of the rates and the energy threshold attainable by the mini-telescope for detection of cosmic rays or gamma-rays in the presence of a given NSB is based on the experience acquired

2020 JINST 15 P04004

during the operation of the SST-1M. The telescope is at the Krakow Institute of Physics (IFJ-Pan), which is sitting close to the largest mall of the city. Light pollution measured during the observation campaigns by the SST-1M camera is quite high, typically around 600 MHz of p.e. rate per pixel, reaching above 1.3 GHz. Hence, the conditions and the values used here are to be considered for high moon and worse than light pollution at Observatories far from cities, such as the one in Saint-Luc, where we took the mini-telescope (see section 4). They are also a bit worse than the NSB level at the Observatory of Geneva in Sauverny, where during observations some lights in buildings were turned on. Surely these values are realistic in case the mini-telescope would be used in an Institute for outreach.

In this section we estimate analytically the expected gamma-ray and cosmic ray signal that the mini-telescope can see in the presence of high NSB.

B.1 Relevant quantities used for estimation

The relevant quantities used for our estimation are reported in table 3 and compared between the SST-1M and the mini-telescope. The solid angle seen by a pixel is: $\Omega_p = 2\pi \left[1 - \cos\left(\frac{d}{2f}\right)\right]$, where the linear size of the pixel is $d = 2.32\,\mathrm{cm}$ (same as for SST-1M) and the focal length of the lens is $f = 2.4\,\mathrm{m}$ (while for the SST-1M mirror $f = 5.6\,\mathrm{m}$).

	A_{eff} [m^2]	f [m]	pixel angle [°]	Ω_p [10^{-5} sr]	$\epsilon_{\mathrm{cam,\ Ch}}$	$\epsilon_{\mathrm{cam,\ NSB}}$	f_{NSB} [GHz (p.e)]
SST-1M	6.50	5.6	0.24	1.3	0.177	0.062	[0.6; 1.5]
Mini-Telescope	0.85	2.4	0.55	7.3	0.195	0.134	[0.9; 1.9]

Table 3. Comparison of relevant quantities for the SST-1M and the mini-telescope. For the SST-1M, A_{eff} is the effective mirror area, after correcting for transmissivity in the Cherenkov signal wavelength region and shadowing from mechanical elements. For the mini-telescope, it is the area of the lens of $1\,\mathrm{m}^2$, reduced by its transmittance of about 85% averaged over the Cherenkov spectrum. The focal length f, the pixel angle, its field of view Ω_p, the camera efficiency for the Cherenkov spectrum, $\epsilon_{\mathrm{cam,\ Ch}}$, and for the typical NSB spectrum, $\epsilon_{\mathrm{cam,\ NSB}}$, the range of NSB rate in p.e. per second and per pixel, f_{NSB}, are indicated.

B.2 Estimation of the night sky background rate

A relevant quantity to determine is the night sky background, f_{NSB} in the table, is the NSB rate induced by the NSB flux on the camera, Φ_{NSB}, which is assumed to be the same for the SST-1M and the mini-telescope. We can calculate the range of Φ_{NSB} from the f_{NSB} range for the SST-1M telescope in Krakow using the following formula:

$$\Phi_{\mathrm{NSB}} = \frac{f_{\mathrm{NSB}}}{A_{\mathrm{eff}} \cdot \Omega_p \cdot \epsilon_{\mathrm{cam,\ NSB}}} \tag{B.1}$$

where the values are provided in table 3. The efficiency of the camera for NSB can be obtained from:

$$\epsilon_{\mathrm{cam,\ NSB}} = \int_{\lambda_{\mathrm{min}}}^{\lambda_{\mathrm{max}}} T_{\mathrm{win}}(\lambda) \cdot T_{\mathrm{lg}}(\lambda) \cdot \mathrm{PDE}(\lambda) \cdot F_{\mathrm{NSB}}(\lambda) \cdot d\lambda \tag{B.2}$$

where $\mathrm{T}_{\mathrm{win}}(\lambda)$ is the transmission of the 2 mm window, $\mathrm{T}_{\mathrm{lg}}(\lambda)$ the transmittance of the light guide, $\mathrm{PDE}(\lambda)$ the photodetection efficiency of the sensor and $\mathrm{F}_{\mathrm{NSB}}(\lambda)$ the NSB fluence. Replacing the

2020 JINST 15 P04004

NSB fluence by the Cherenkov one in eq. (B.2) allows deriving the efficiency of the camera for the Cherenkov spectrum $\epsilon_{\text{cam, Ch}}$. The calculation gives the results that are listed in table 3. The differences observed between the SST-1M camera and the mini-camera only come from their protection windows. The SST-1M window has a low pass filter coating with a cut-off at 540 nm. The mini-camera window is made of PMMA (poly methyl methacrylate) which has a better transmissivity below 300 nm, but does not have any filter. However, we cannot use these values to compute Φ_{NSB}, as they were measured in dark conditions. As explained in section 3, high NSB affects the properties of SiPMs, and in particular reduces the PDE, the sensor gain and the optical cross talk. A detailed estimate is shown in ref. [32]. Also, in ref. [39], one can see that the PDE does not decrease equally with respect to the over-voltage depending on the wavelength considered. In order to simplify the calculation, we will derive the PDE variation for the average wavelength of both spectra, i.e. 415 nm for Cherenkov and 651 nm for NSB. From [32], we find out that at 600 MHz (1.5 GHz) the PDE decreased by 15% (30%) for both wavelengths. Therefore, $\epsilon_{\text{cam, NSB}}(600\,\text{MHz}) = 0.053$ and $\epsilon_{\text{cam, NSB}}(1.5\,\text{GHz}) = 0.043$. Using eq. (B.1) we obtain $\Phi_{\text{NSB}} \in [1.3,\ 3.3] \times 10^{15}$ photons/(m^2 s sr), which we assume the same that impinges on the mini-camera. Hence, using the mini-camera parameters in table 3, we can derive $f_{\text{NSB}} \in [0.9,\ 1.9]$ GHz for the mini-camera.

B.3 Estimation of the Cherenkov photons density

We make a rough estimate of the significance, namely the number of sigmas of a gamma-ray signal at ground level with respect to night sky background:

$$N_\sigma = \frac{\text{signal}}{\sqrt{\text{noise}}} = \frac{d_{\text{ch}} \times A_{\text{eff}} \times T \times \epsilon_{\text{cam, Ch}}}{\sqrt{\Phi_{\text{NSB}} \times A_{\text{eff}} \times T \times \tau \times \Omega \times \epsilon_{\text{cam, NSB}}}} \tag{B.3}$$

where d_{ch} is the density of Cherenkov photons from an electromagnetic shower induced by a photon of energy E_γ; Φ_{NSB} is the NSB flux provided above; Ω is the solid angle corresponding to the field of view of the mini-camera obtained as $\Omega = \Omega_p \times N_{\text{ch}}$, with N_{ch} number of camera channels. We neglect the transmittance of the atmosphere setting it to $T = 1$. The lens effective area is $A_{\text{eff}} = 0.85\,\text{m}^2$; $\tau = 20$ ns is the time during which the ASIC searches for the maximum of the signal (FPGA hold delay in figure 6). After this period, the found maximum value is stored in analog memories and it cannot be overwritten during the next 9.12 µs, so it is not able to measure additional charge. Therefore, only the photons that come within this time window of 20 ns affect the measurement of the Cherenkov signal. By requiring that a signal-to-noise ratio of 5σ is achieved to detect signal, we estimate the needed number of Cherenkov photons per unit surface:

$$d_{\text{ch}} = \frac{N_\sigma}{\epsilon_{\text{cam, Ch}}} \cdot \sqrt{\frac{\Phi_{\text{NSB}} \cdot \tau \cdot \Omega \cdot \epsilon_{\text{cam, NSB}}}{A_{\text{eff}} \cdot T}} \simeq 5\text{'}773 - 10\text{'}288\,\text{photons/m}^2 \tag{B.4}$$

B.4 Estimation of the cosmics rays energy threshold

With this definition of detectable signal over background, we extract a minimum photon energy for the shower to be detectable of $E^\gamma_{\text{Th}} = 42$–$68$ TeV from figure 19-left. This plot was obtained as shown in the appendix section A. The plot in figure 19-right shows the ratio between the energy of a proton and a gamma-ray giving the same density of Cherenkov photons, as obtained by CORSIKA simulations (see ref. [40]). At 42–68 TeV, this ratio is about 2.7–2.6 translating into a minimal energy threshold for detecting cosmic rays of $E^p_{\text{Th}} \sim 113$–177 TeV for the mini-telescope.

2020 JINST 15 P04004

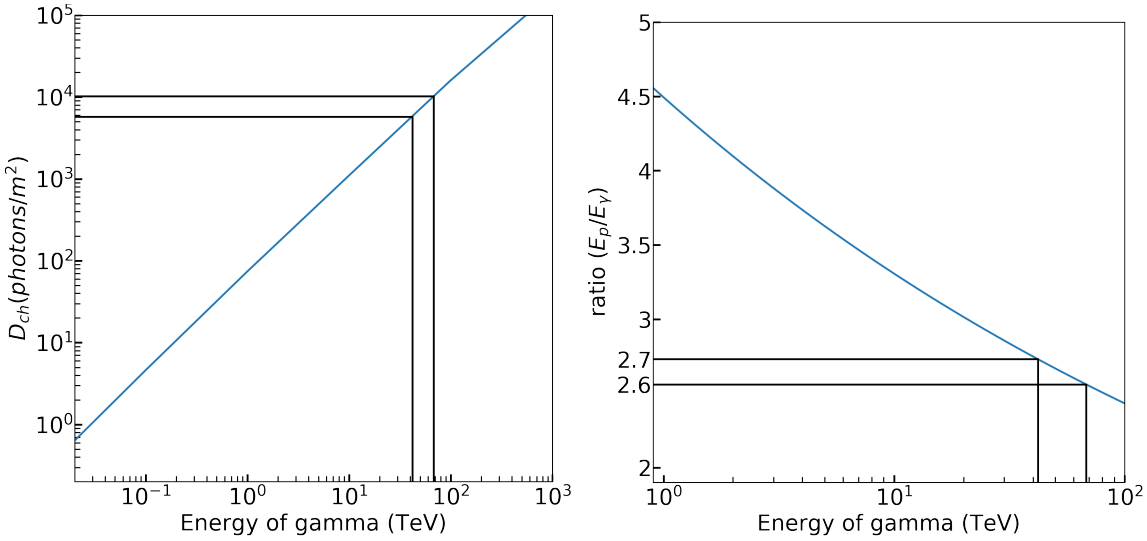

Figure 19. *Left*: density at sea level of the Cherenkov photons as a function of the energy of the primary gamma-ray producing the electromagnetic shower (see the appendix). *Right*: ratio between the energy of a proton and of a gamma-ray producing the same density of photons at ground as a function of the primary energy.

B.5 Estimation of the cosmics rays shower rate

Considering the analytical function describing the differential flux in energy of all-nucleon cosmic rays from ref. [38]:

$$I = 1.8 * 10^4 * E^{-2.7} = \frac{dN}{dE\ d\Omega\ dS\ dt} \tag{B.5}$$

the rate can be estimated integrating this flux for energies above 113 TeV up to 500 TeV.[2] Given that the light pool produced by a shower in this energy range extends dominantly over a radius of about $R \sim 130$ m at sea level [2], we can calculate the cosmic ray shower rate on the mini-telescope as

$$\text{rate} = \int_{E>113\times10^3\,\text{GeV}} \frac{dN}{dE\ d\Omega\ dS} dE \times \Omega \times \pi R^2 \sim 0.014\,\text{Hz} \tag{B.6}$$

where Ω is the solid angle corresponding to the field of view of the telescope.

C The Graphical User Interface

Designing an user-friendly Graphical User Interface (GUI) is particularly important for this project, especially if used for outreach. The GUI has to be of easy and immediate use, but it needs to provide access to all the features of the system. The software has been coded in Python and has been designed to simplify as much as possible the number of parameters to be managed by the user. The GUI has two main panels (see figure 20): the configuration panel and the display window. The configuration panel allows to manage the threshold parameters of the ASIC and the FPGA as the

[2]Above 500 TeV the rate of events would be negligible in the mini-telescope and anyway assuming 1 PeV as upper limit the result changes very slightly.

2020 JINST 15 P04004

energy threshold, the number of coincidences on the neighboring pixels for the trigger condition, the display mode of the charge (measured in ADC value or photo-electron, indicated as p.e.) in the pixels. The GUI is also interfaced to the data acquisition software, collecting data through a server directly connected to the FEB via USB3 interface. The display window can show in real time the image of the shower of highest energy acquired during a programmable time interval. Additionally, it can show a temperature map, i.e. the temperature measured by all available pixels. Through the GUI, it is also possible to make some histograms for each pixel and also to plot the data rate during the trigger scans.

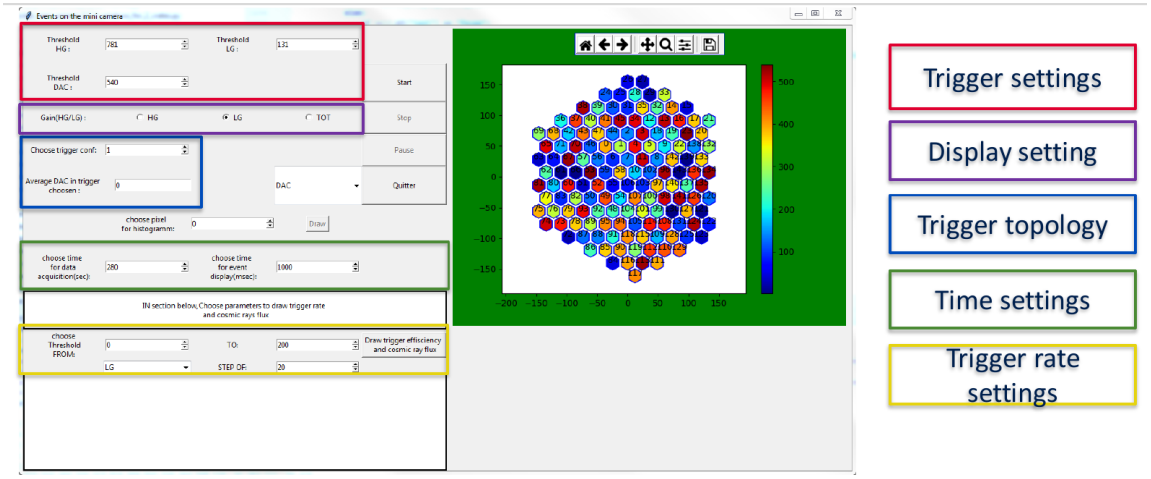

Figure 20. The Graphical User Interface.

References

[1] J. Matthews, *A Heitler model of extensive air showers*, *Astropart. Phys.* **22** (2005) 387.

[2] M. de Naurois and D. Mazin, *Ground-based detectors in very-high-energy gamma-ray astronomy*, *Compt. Rendus Physique* **16** (2015) 610 [arXiv:1511.00463].

[3] T.C. Weekes et al., *Observation of TeV gamma rays from the Crab nebula using the atmospheric Cerenkov imaging technique*, *Astrophys. J.* **342** (1989) 379.

[4] HESS collaboration, *The H.E.S.S. Galactic plane survey*, *Astron. Astrophys.* **612** (2018) A1 [arXiv:1804.02432].

[5] MAGIC collaboration, *The major upgrade of the MAGIC telescopes, Part II: A performance study using observations of the Crab Nebula*, *Astropart. Phys.* **72** (2016) 76 [arXiv:1409.5594].

[6] VERITAS collaboration, *Performance veritas*, (2019) https://veritas.sao.arizona.edu/about-veritas-mainmenu-81/veritas-specifications-mainmenu-111.

[7] H. Abdalla et al., *A very-high-energy component deep in the γ-ray burst afterglow*, *Nature* **575** (2019) 464 [arXiv:1911.08961].

[8] MAGIC collaboration, *Teraelectronvolt emission from the γ-ray burst GRB 190114C*, *Nature* **575** (2019) 455.

2020 JINST 15 P04004

[9] MAGIC collaboration, *Observation of inverse Compton emission from a long γ-ray burst*, *Nature* **575** (2019) 459.

[10] S. Wakely and D. Horan, *Tevcat*, (2020) http://tevcat.uchicago.edu/.

[11] S.P. Wakely and D. Horan, *TeVCat: An online catalog for Very High Energy Gamma-Ray Astronomy*, in proceedings of the *30th International Cosmic Ray Conference (ICRC 2007)*, Merida, Yucatan, Mexico, 3–11 July 2007, volume 3, pp. 1341–1344 and online at http://indico.nucleares.unam.mx/contributionDisplay.py?contribId=378&confId=4.

[12] CTA Observatory, (2020) https://www.cta-observatory.org/.

[13] CTA Consortium collaboration, *Science with the Cherenkov Telescope Array*, World Scientific (2017), arXiv:1709.07997.

[14] CTA and SST-1M collaborations, *The small size telescope projects for the Cherenkov Telescope Array*, PoS(ICRC2015)1043 (2016) [arXiv:1508.06472].

[15] M. Heller et al., *An innovative silicon photomultiplier digitizing camera for gamma-ray astronomy*, *Eur. Phys. J.* **C 77** (2017) 47 [arXiv:1607.03412].

[16] SST-1M sub-Consortium, *Design, optimization and characterization of the light concentrators of the single-mirror small size telescopes of the Cherenkov Telescope Array*, *Astropart. Phys.* **60** (2015) 32 [arXiv:1404.2734].

[17] HAWC, (2020) https://www.hawc-observatory.org.

[18] LHAASO collaboration, *The LHAASO experiment: from Gamma-Ray Astronomy to Cosmic Rays*, *Nucl. Part. Phys. Proc.* **279–281** (2016) 166 [arXiv:1602.07600].

[19] G. Cusumano et al., *GAW (Gamma Air Watch): A Novel imaging Cherenkov telescope*, astro-ph/0110572.

[20] JEM-EUSO collaboration, *The JEM-EUSO program*, arXiv:1703.01875.

[21] M. Heller et al., *The SST-1M project for the Cherenkov Telescope Array*, in proceedings of the *36th International Cosmic Ray Conference (ICRC2019)*, Madison, WI, U.S.A. 24 July–1 August 2019, PoS(ICRC2019)694 (2019).

[22] M. Antonova et al., *The Baby MIND spectrometer for the J-PARC T59(WAGASCI) experiment*, PoS(EPS-HEP2017)508 (2017).

[23] Hamamatsu, (2020) https://www.hamamatsu.com.

[24] J.A. Aguilar et al., *The front-end electronics and slow control of large area SiPM for the SST-1M camera developed for the CTA experiment*, *Nucl. Instrum. Meth.* **A 830** (2016) 219.

[25] Weeroc, *Datasheet Citiroc1A*, (2019) and online pdf version at https://www.weeroc.com/my-weeroc/download-center/citiroc-1a/16-citiroc1a-datasheet-v2-5/file.

[26] E. Noah et al., *Readout scheme for the Baby-MIND detector*, in proceedings of the *4th International Conference on New Photo-Detectors (PhotoDet 2015)*, Moscow, Russian Federation, 6–9 July 2015, PoS(PhotoDet2015)031 (2016).

[27] O. Basille et al., *Baby MIND Readout Electronics Architecture for Accelerator Neutrino Particle Physics Detectors Employing Silicon Photomultipliers*, *JPS Conf. Proc.* **27** (2019) 011011.

[28] E. Noah et al., *The WAGASCI experiment at JPARC to measure neutrino cross-sections on water*, PoS(EPS-HEP2015)292 (2015).

2020 JINST 15 P04004

[29] Y. Takizawa, *The TA-EUSO and EUSO-Balloon optics designs*, in proceedings of the *33rd International Cosmic Ray Conference (ICRC 2013)*, Rio de Janeiro, Brazil, 2–9 July 2013.

[30] A. Nagai et al., *Characterisation of a large area silicon photomultiplier*, arXiv:1810.02275.

[31] I. Al Samarai et al., *Calibration and operation of SiPM-based cameras for gamma-ray astronomy in presence of high night-sky light*, arXiv:1908.06860.

[32] A. Nagai et al., *SiPM behaviour under continuous light*, 2019 *JINST* **14** P12016 [arXiv:1910.00348].

[33] CTA SST-1M Project collaboration, *Performance of a small size telescope (SST-1M) camera for gamma-ray astronomy with the Cherenkov Telescope Array*, PoS(ICRC2017)758 (2018) [arXiv:1709.03914].

[34] K. Bernlöhr, *Simulation of Imaging Atmospheric Cherenkov Telescopes with CORSIKA and sim_telarray*, *Astropart. Phys.* **30** (2008) 149 [arXiv:0808.2253].

[35] I. de la Calle Perez and S.D. Biller, *Extending the sensitivity of air Cerenkov telescopes*, *Astropart. Phys.* **26** (2006) 69 [astro-ph/0602284].

[36] SERI, *Swiss government excellence scholarships for foreign scholars and artists*, (2020) https://www.sbfi.admin.ch/sbfi/en/home/education/scholarships-and-grants/swiss-government-excellence-scholarships.html.

[37] W. Heitler, *Quantum theory of radiation*, Dover Publications (1954).

[38] Particle Data Group, *Review of Particle Physics*, *Phys. Rev.* **D 98** (2018) 030001.

[39] A. Nagai et al., *Characterisation of a large area silicon photomultiplier*, *Nucl. Instrum. Meth.* **A 948** (2019) 162796.

[40] P. Hazarika, G.S. Das and U.D. Goswami, *Parameterisation of lateral density and arrival time distributions of Cherenkov photons in EASs as functions of independent shower parameters for different primaries*, arXiv:1807.09471.

2020 JINST 15 P04004